1   **Single-Crystal Equations of State of Magnesiowüstite at High Pressures**

2   **(Revision 1)**

3   Gregory J. Finkelstein[1*], Jennifer M. Jackson[1], Wolfgang Sturhahn[1], Dongzhou Zhang[2], E. Ercan

4   Alp[3], Thomas S. Toellner[3]

5   [1]Seismological Laboratory, California Institute of Technology, 1200 E. California Blvd., MS

6   252-21, Pasadena, California 91125, USA

7   [2]Partnership for Extreme Crystallography, University of Hawaii, School of Ocean and Earth

8   Science and Technology, University of Hawaii, 1680 East West Road (POST Bldg 819E),

9   Honolulu, Hawaii 96822, USA

10   [3]Advanced Photon Source, Argonne National Laboratory, 9700 South Cass Avenue, Argonne,

11   Illinois 60439, USA

12   *Email Address: gjfinkel@gps.caltech.edu

13

14

15

16

17

18

19   Keywords: magnesiowüstite, single-crystal diffraction, elasticity, equations of state, Mössbauer

20   spectroscopy, high pressure

21

22

23

24   **Abstract**

25   Solid solutions of (Mg,Fe)O with high iron enrichment may be an important component of

26   ultralow-velocity zones at Earth's core-mantle boundary. However, to date there have been few

27   high-precision studies on the elastic properties of these materials. In this study we present results

28   on the compression of $(Mg_{0.22}Fe_{0.78})O$ magnesiowüstite in both neon and helium pressure media

29   using single-crystal diffraction to ~55 GPa. In addition, our sample was characterized by time-

30   domain synchrotron Mössbauer spectroscopy at ambient pressure using an extended time range

31   that resulted in vastly improved energy resolution. The combination of these high-resolution

32   techniques tightly constrains the presence of a defect-structure component at room pressure due

33   to 4.7 mol% tetrahedrally-coordinated ferric iron, resulting in a renormalized composition of

34    $(Mg_{0.215}Fe_{0.762}\square_{0.023})O$. Both high-pressure diffraction datasets are well described by a 3rd-order

35   Birch-Murnaghan equation of state. The best fit-parameters for a crystal with cubic structure in

36   helium are $K_{0T} = 148(3)$ GPa, $K'_{0T} = 4.09(12)$, and $V_0 = 78.87(6)$ $Å^3$. Increasing differential

37   stress in the neon-containing sample chamber was correlated with increasing apparent distortion

38   of the initially cubic unit cell, requiring a lower-symmetry hexagonal cell to fit the data above

39   ~20 GPa. For fit equations of state, we determine the pressure-dependent correlation ellipses for

40   the equation of state parameters and compare with previously published single-crystal diffraction

41   data from (Mg,Fe)O crystals in a helium medium. We make two main observations from the

42   datasets using a helium pressure medium: K_{0T} decreases as a function of increasing iron content

43   from periclase to wüstite and K'_{0T} is consistent with an approximately constant value of 4.0 that

44   is independent of iron content, at least up to (Mg,Fe)O containing ~78 mol% FeO. In

45   combination with previously reported thermal parameters, we compute the density of Mw78 at

46   core-mantle boundary conditions and discuss the implications.

47

Introduction

49

50 Ferromagnesian oxides are a primary component of the earth's lower mantle, along with the

51 dominant bridgmanite and minor $CaSiO_3$ perovskite phases (Irifune 1994; Tschauner et al.

52 2014). While the bulk of the lower mantle likely contains (Mg,Fe)O ferropericlase solid

53 solutions with ~10-40mol% of FeO (Fei et al. 1996; H. Mao 1997; Sinmyo et al. 2008), the

54 presence of material significantly more enriched in Fe has been hypothesized as an explanation

55 for some of the complex seismic structure observed near the core-mantle boundary (CMB). In

56 particular, ultralow-velocity zones (ULVZs), 10s of km-thick patches at the CMB, show a ~10%

57 reduction in seismic P-wave velocity and a ~30% reduction in seismic S-wave velocity from

58 average lower-mantle values (Wen 1998; Thorne and Garnero 2004; Rost et al. 2006).

59

60 While a number of suggestions have been put forth in the literature to explain the origin of these

61 features (Manga and Jeanloz 1996; Williams et al. 1998; W. L. Mao et al. 2006), one hypothesis

62 that has gained traction in recent years proposes Fe-rich oxide components to explain the

63 observed low sound velocities. Work by Wicks et al. (2010) used nuclear resonant inelastic

64 scattering to show that the shear velocity of $(Mg_{0.16}Fe_{0.84})O$ magnesiowüstite was ~55% slower

65 than endmember MgO at CMB pressures, and that only ~10 vol. % of this material mixed with a

66 silicate assemblage would be needed to match ULVZ seismic velocities. Subsequent simulations

67 (Bower et al. 2011) that explored the geodynamic effects of enriching ULVZ material with

68 magnesiowüstite produced morphologies consistent with observed ULVZ seismic topography

69 (Sun et al. 2013).

3

70

71   While selected properties of (Mg,Fe)O with low iron concentrations have been determined at

72   pressures above 1 Mbar and temperatures over 2000 K (Westrenen et al. 2005; Lin et al. 2006;

73   2007; Z. Mao et al. 2011), until recently, the iron-rich members of this solid solution received

74   less attention (Ohta et al. 2014; Wicks et al. 2015; 2017), and still little is known about their

75   crystallographic and elastic properties. At ambient conditions, all (Mg,Fe)O solid solutions

76   crystallize in the cubic B1 structure. Single-crystal x-ray diffraction (SXRD) has shown,

77   however, that endmember wüstite, FeO, undergoes a slight rhombohedral distortion from cubic

78   symmetry at ~18-23 GPa and 300 K (Hazen and Jeanloz 1984; Shu et al. 1998; Jacobsen et al.

79   2005), whereas $(Mg_{0.73}Fe_{0.27})O$ remains cubic to at least 51 GPa (Jacobsen et al. 2005). A

80   powder diffraction (PXRD) study on $(Mg_{0.22}Fe_{0.78})O$ reported a rhombohedral transition at 20-40

81   GPa (Zhuravlev et al. 2010), whereas a PXRD study on $(Mg_{0.06}Fe_{0.94})O$ bracketed the cubic to

82   rhombohedral transition between 13 and 24 GPa (Wicks et al. 2015). The rhombohedral

83   distortion may also be associated with a magnetic transition at or near the structural transition

84   pressure (Struzhkin et al. 2001; Jacobsen and Spetzler 2004; Kantor et al. 2004; Wicks et al.

85   2010).

86

87   Diffraction methods are generally used in compression experiments to probe the volume

88   reduction of the crystallographic unit cell with pressure, and thus bulk compressibility, as well as

89   any structural transitions that may occur. Pressure-volume relationships are frequently modeled

90   with an equation of state, which results in an estimate of a material's isothermal bulk modulus,

91   K_T, as well as its pressure derivative, K'_T. When constrained well by the measured data, these

4

92   parameters can be used in the calculation of sound velocities and density profiles and then

93   compared to observed seismic data.

94

95   In a high-pressure apparatus such as a diamond anvil cell, where sample dimensions are

96   frequently limited to tens of microns, diffraction from powdered samples often suffers from poor

97   grain statistics, has difficult-to-fit overlapping peaks, and the scattered intensity is significantly

98   weaker than that of similarly-sized single crystals. Combined, these effects tend to result in

99   increased data scatter of compression curves measured from powdered samples compared with

100   those from single crystals. Therefore, in order to more conclusively determine its compression

101   behavior, here we expand on the previous study of ground, polycrystalline $(Mg_{0.22}Fe_{0.78})O$ by

102   compressing and measuring the SXRD of single crystals drawn from the same batch of sample

103   used in the earlier work. Furthermore, we evaluate the influence of the pressure medium by

104   running experiments in two different commonly used quasihydrostatic media: neon and helium.

105   We complement the SXRD measurements with high-resolution time-domain synchrotron

106   Mössbauer spectroscopy to tightly constrain the ferric iron concentration, which coupled with

107   diffraction data, helps constrain the defect concentration.

108

109   **Experimental Procedures**

110

111   We prepared two diamond-anvil cells (DAC) for high-pressure experiments. One cell was a

112   standard Princeton-design symmetric DAC with a cubic boron nitride seat on the cylinder side

113   and a tungsten carbide seat on the piston side. Standard modified brilliant-cut diamond anvils

114   with flat 300 µm culets were used on both seats. The other DAC was a BX90 cell (Kantor et al.

115   2012) with symmetric Boehler-Almax-geometry seats (Boehler and De Hantsetters 2007) and

116   diamonds with 250 µm beveled culets. Each cell's ~40 µm thick rhenium gasket was loaded with

117   a nearly identical sample configuration that consisted of two or three <10 µm thick ruby sphere

118   pressure calibrants and platelets of synthetic $(Mg_{0.22}Fe_{0.78})O$ magnesiowüstite, hereafter referred

119   to as Mw78, <10 µm in thickness and ~20-30 µm in diameter. These small pieces were broken

120   off from a larger single crystal. Additional details regarding the synthesis and characterization of

121   this sample material may be found in previous publications (Jacobsen 2002; Mackwell et al.

122   2005). The prepared DACs were subsequently gas-loaded with neon (symmetric DAC) or helium

123   (BX90 DAC) pressure media at ~25,000 PSI using either the Caltech or COMPRES/GSECARS

124   gas-loading system (Rivers et al. 2008), respectively (see supplementary information for images

125   of sample chambers at high pressure).

126

127   The ambient diffraction pattern of a portion of the magnesiowüstite sample was characterized at

128   the 11.3.2 beamline of the Advanced Light Source at Lawrence Berkeley National Laboratory (λ

129   = 0.6702 Å). Single crystal diffraction measurements at high pressures were collected on each

130   DAC sample configuration at the Advanced Photon Source at Argonne National Laboratory. The

131   He-medium experiment was conducted at the PX^2 BM-C beamline (λ = 0.4340 Å) and the Ne-

132   medium experiment at the ID-D beamline (λ = 0.3100 Å) of the GSECARS sector. We achieved

133   maximum pressures of 55.9(3) and 53.0(1.5) GPa, respectively. Downstream X-ray opening

134   angles of the loaded cells were determined to be 48° (Ne) and 60° (He). The number of measured

135   diffraction peaks at each pressure point is determined by lattice-parameter lengths, x-ray energy,

136   and opening angle of the diamond anvil cell. After each pressure increase, the cell was allowed

137   to rest for at least 20 minutes before collection of diffraction, minimizing pressure creep. Ruby

138   spectra were obtained immediately after the diffraction patterns were collected for a given

139   compression step. Several experiments using similar methods for the collection of single crystal

140   diffraction patterns at high pressure can be found in the recent literature, providing additional

141   details on the procedure (Dera et al. 2013a; Finkelstein et al. 2014).

142

143   Experimental pressures were determined using the ruby scale of Dewaele et al. (2004). The

144   uncertainty in pressure at each step was estimated as the standard deviation of the pressures

145   measured for the different rubies in each sample chamber. Diffraction peaks were fit and lattice

146   parameters refined in either the APEX 2 (ambient measurements) (Bruker 2012a) or the

147   GSE_ADA/RSV (high-pressure measurements) (Dera et al. 2013b) software package. Unit cells

148   were indexed based on an analysis of reciprocal lattice difference vectors within the RSV

149   interface using the CELL_NOW (Bruker 2012b) program to (refer to discussion below and

150   supplementary information for example images of indexed reciprocal lattices and unique

151   diffraction peaks used). After converting lattice parameters to unit cell volumes, a 3rd order

152   Birch-Murnaghan equation of state was fit to the pressure-volume data of each experimental run

153   using the MINUTI software package (version 2.0) (Sturhahn 2015b). The 3rd order Birch-

154   Murnaghan equation of state takes the form:

155

$$P(V) = \frac{3K_{0T}}{2}\left[\left(\frac{V_0}{V}\right)^{\frac{7}{3}} - \left(\frac{V_0}{V}\right)^{\frac{5}{3}}\right]\left\{1 + \frac{3}{4}(K'_{0T} - 4)\left[\left(\frac{V_0}{V}\right)^{\frac{2}{3}} - 1\right]\right\}$$

156

157   The parameters of pressure, unit cell volume, zero-pressure unit cell volume, and isothermal

158   zero-pressure bulk modulus and its pressure derivative are represented by the symbols P, V, V_0,

159   K_{0T}, and K'_{0T}, respectively. Using a new feature of MINUTI, we computed the covariance matrix

160   of each of our equation of state fits as a function of pressure. The covariance matrices were used

161   to calculate 68% and 95% confidence ellipses for our fit equation of state parameters, also as a

162   function of pressure (Sturhahn 2015b); the reader is also referred to Angel (2000) for more

163   information on covariance matrices and confidence ellipses as they relate to equations of state as

164   a function of pressure.

165

166   To complement our diffraction experiments and aid in the determination of the ferric content of

167   our sample, we applied synchrotron Mössbauer spectroscopy (SMS) at APS Sector 3-ID-B in

168   hybrid top-up mode. The measured single-crystalline platelet of Mw78 was ~110 μm thick,

169   resulting in an effective thickness of about 10. The x-rays were focused to ~10 x 11 μm^2 (D.

170   Zhang et al. 2015), and a high-resolution monochromator provided an energy bandwidth of 1

171   meV at the 14.4125 keV [57]Fe nuclear transition energy (Toellner 2000). The SMS spectrum was

172   fit using the CONUSS software package (Sturhahn 2015a). With our use of APS hybrid mode, a

173   time range of 35 ns to 860 ns became accessible for the SMS spectrum. This extended time range

174   translates into a much improved energy resolution of about 1.1 Γ (Γ = 4.66 neV is the natural line

175   width of the 14.4125 keV [57]Fe nuclear excited state) which compares to >2 Γ for conventional

176   Mössbauer experiments using a radioactive source (Sturhahn 2001, Eq. 13). At present,

177   experiments using the hybrid mode require long data collection times due to limited useful x-ray

178   intensity. Therefore, our SMS spectrum collected with the extended time range took about 20

179   hours of beamtime. However, there is a clear advantage in taking SMS spectra in hybrid mode.

180   Out of the various kinds of Mössbauer spectroscopy, this configuration has the best energy

8

181 resolution to date, leading to markedly improved accuracy in the fit of potential minor sites and

182 to finely resolved small differences in hyperfine parameters.

183

184 **Room-Pressure Results and Discussion**

185

186 At ambient conditions, the Mw78 crystal can be nominally indexed with a cubic unit cell (Table

187 1). However, upon closer examination of the diffraction peaks at long exposure times, faint,

188 diffuse satellites are observed around the primary peaks, with their intensity significantly

189 decreasing at high two-theta angles (Figure 1). This additional scattering has been observed in

190 several previous studies on the wüstite endmember (Hazen and Jeanloz 1984; Jacobsen et al.

191 2005), but has not previously been reported for (Mg,Fe)O solid solutions. The complex intensity

192 distribution around the satellite peaks of wüstite has been interpreted as being directly related to

193 an inhomogeneous paracrystalline structure that consists of regions of high defect-cluster density

194 and regions of low defect-cluster density (Welberry and Christy 1997; Saines et al. 2013). As the

195 observed scattering due to the defect structure is extremely weak, in this paper we use the Bragg

196 peak positions alone to determine lattice parameter values, even though we recognize that they

197 do not fully describe the sample's structure.

198

199 By fitting an SMS spectrum from our sample, we were able to quantify its ferric and ferrous

200 components. While the bulk (Mg,Fe)O structure is composed of octahedrally-coordinated ferrous

201 Fe, the defect structure is thought to be made of clusters of tetrahedrally-coordinated ferric Fe.

202 These two types of Fe can be readily distinguishable in an SMS spectrum, as the hyperfine fields

9

203   (e.g. isomer shift, quadrupole splitting) are sensitive to both oxidation state and coordination

204   number.

205

206   Previously published SMS and conventional Mössbauer studies on $(Mg,Fe)O$ and wüstite (e.g

207   Johnson et al. (1969), Lin et al. (2006), McCammon et al. (1985), and Solomatova et al. (2016))

208   have used several different models to fit the complex observed spectra, ranging from a single

209   doublet (Lin et al. 2006) to multiple doublets and singlets (McCammon and Price 1985). After

210   investigating these and similar models, we concluded that our spectrum required a model with

211   four Fe sites to achieve an optimal and physically meaningful fit. These four sites consist of three

212   doublets and one singlet. The SMS spectrum was collected without an external reference

213   standard, such as a stainless steel foil, which would permit determination of all isomer shifts.

214   However, by fixing three of the doublets to an isomer shift of 1.0 mm/s (a value that is

215   reasonable for an octahedrally-coordinated ferrous Fe site), we determine the relative isomer

216   shift of the fourth site. Combined, the three doublet sites correspond to ~94% of the Fe sites, and

217   have quadrupole splitting values ranging from 0.6 to 1.3 mm/s (Table 1). In light of this

218   information, we assign the three doublets to high-spin ferrous sites. The singlet, on the other

219   hand, exhibited an isomer shift ~0.95 mm/s lower than the other sites, which is consistent only

220   with tetrahedrally-coordinated high-spin ferric Fe (Dyar et al. 2006). This interpretation is

221   distinct from select Mössbauer studies on wüstite, where the singlet site was interpreted as a

222   component of the metallic iron sextet (McCammon and Price 1985). Renormalizing the

223   measured Mw78 sample composition to take into account the vacancies necessitated by the ferric

224   Fe content results in a composition of $(Mg_{0.215}Fe(II)_{0.716} Fe(III)_{0.046}\ _{0.023})O$ if ferric and ferrous

225   Fe are separated in the chemical formula, and $(Mg_{0.215}Fe_{0.762}\ _{0.023})O$ if not distinguished.

10

226

High-Pressure Results and Discussion

Phase Stability (subsection)

At low pressures, the Mw78 crystal in neon has a diffraction pattern that can be indexed with the

expected cubic unit cell. At high pressures, the diffraction peak positions are no longer

compatible with this unit-cell geometry, and a lower-symmetry cell is required. We do not see

evidence for twinning in the high-pressure phase. With the obtained coverage of reciprocal

space, a hexagonal unit cell is sufficient for fitting the observed unit cell distortion. Deviations

from cubic symmetry can be quantified by monitoring the c/a lattice parameter ratio. Figure 3a

(bottom) shows the pressure dependence of the c/a ratio which has a value of $\sqrt{6} \approx 2.45$ for a

cubic material. A Mw78 crystal in neon remains cubic until ~20 GPa, above which it becomes

increasingly hexagonal (as observed by analysis of the reciprocal lattice difference vectors – see

Figure 3b). In contrast, a Mw78 crystal in the helium pressure medium gives a c/a ratio near 2.45

over the whole pressure range, indicating that the unit cell remains metrically cubic up to the

maximum pressure of our study. Lattice parameter values refined in both the cubic and

hexagonal settings are provided in Table 2.

Previous high-pressure studies on $(Mg_{0.22}Fe_{0.78})O$ and $(Mg_{0.06}Fe_{0.94})O$ in neon reported

rhombohedral transitions around 20-40 GPa and 13-24 GPa, respectively (Zhuravlev et al. 2010).

These results are compatible with our result on Mw78 in neon. High-pressure studies of helium-

loaded wüstite single crystals (Shu et al. 1998; Jacobsen et al. 2005) reported fourfold non-

merohedral twinning inherent to the mechanism of a rhombohedral transition in wüstite. Our

single-crystal diffraction study on Mw78 in helium shows no evidence for a lower symmetry

11

249   distortion up to 55 GPa. The addition of MgO to wüstite appears to prevent such a transition and

250   to extend the stability field of the cubic phase.

251

252   Since ruby spheres were placed in several locations inside the sample chamber of each DAC

253   (refer to supplementary figures for pictures), we were able to use the standard deviation of the

254   calibrated ruby pressures as a proxy for nonhydrostaticity experienced by the sample. As seen in

255   Figure 3a (top), this quantity remains near zero for the helium-loaded sample chamber, but

256   rapidly increases in the neon-loaded sample chamber above ~20 GPa. The nonhydrostaticity

257   proxy shows the exact same pressure dependence as the hexagonal distortion of Mw78 described

258   earlier. Previous work also investigated the quasihydrostatic pressure limits of helium and neon

259   media using the ruby standard deviation method up to ~40 and ~50 GPa, respectively (Klotz et

260   al. 2009). Their results suggest that while nonhydrostaticity in a neon medium increases rapidly

261   above ~15 GPa, nonhydrostaticity in a helium medium increases gradually above ~23 GPa.

262

263   **Equations of State (subsection)**

264   Figure 4 shows compression curves for single-crystalline Mw78 in helium (indexed as cubic)

265   and neon (indexed as cubic and hexagonal), and for powdered $(Mg_{0.22}Fe_{0.78})O$ in neon

266   (Zhuravlev et al. 2010) (indexed as cubic). There is a discernible difference between the Mw78

267   in neon and in helium, as the Mw78 sample in helium is more compressible than those in neon.

268   The compression curves are smooth for each phase and are each well described by a 3rd order

269   Birch-Murnaghan equation of state. Our optimization procedure using the MINUTI software

270   (Sturhahn 2015b) incorporated the measured ambient unit cell volume of 78.94±0.1 Å^3 for our

271   single-crystal cubic-indexed measurements as a prior on V_0. For the crystal in helium, the other

12

272   parameters, K_{0T}, and K'_{0T}, were allowed to vary freely. For the crystal in neon, due to the limited

273   number of data points in respective phase regions, a strong prior of ± 0.1 was put on K'_{0T} for both

274   the cubic (1.3-19.2 GPa) and hexagonal (24.1-53.3 GPa) phases. The best fits to the data were

275   achieved with V_0, K_{0T}, and K'_{0T} values of 78.742(14) Å^3, 163.0(1.0) GPa, and 4.02(10) for the

276   cubic-indexed single crystal Mw78 in neon and 78.87(6) Å^3, 148(3) GPa, and 4.09(12) for the

277   cubic-indexed single crystal Mw78 in helium, V_0, K_{0T}, and K'_{0T} values of 78.5(2) Å^3, 166(5)

278   GPa, and 4.01(10) for the cubic-indexed powdered Mw78 in neon, and V_0, K_{0T}, and K'_{0T} values

279   of 58.7(4) Å^3, 176.8(1.1) GPa, and 4.00(10) for the hexagonal-indexed single crystal Mw78 in

280   neon. These fits are plotted in Figure 4. While both single-crystal cubic compression curves have

281   similar K_{0T}' values (~4), the cubic phase of the sample in neon exhibits a significantly higher

282   value for K_{0T} compared with the sample in helium. This corresponds to higher values of V/V_0 for

283   the sample in neon at pressures above ~5 GPa (Figure 4), and is consistent with Mw78 being

284   very sensitive to nonhydrostaticity, as neon crystallizes at ~4.8 GPa (Klotz et al. 2009). While in

285   our diffraction experiments we cannot confidently resolve a hexagonal distortion in Mw78 until

286   above ~20 GPa, the unit cell volume appears to be affected by neon crystallization below ~20

287   GPa.

288

289   In order to provide context for our results, we re-evaluated equations of state for data on several

290   (Mg,Fe)O compositions using MINUTI or direct comparison with our study (Table 3). Pressure-

291   volume data were sourced from single-crystal diffraction studies by Jacobsen et al. (2002; 2005;

292   2008) and a powder diffraction study by Zhuravlev et al. (2010). Since Zhuravlev et al. (2010)

293   did not collect data near zero pressure, we applied a prior of 4.0 ± 0.1 on K'_{0T} in the equation of

294   state fit. The Jacobsen et al. (2005) data on $Fe_{0.93}O$ covered a limited pressure range, and

13

295   therefore we also applied a prior of 4.0±0.1 on K'_{0T}. This value is consistent with the given

296    $Fe_{0.93}O$ data, as well as with the Mw78 single-crystal diffraction measurements in helium. All

297   other parameters remained unconstrained during fitting.

298

299   All examined (Mg,Fe)O datasets are fit well by a 3rd order Birch-Murnaghan equation of state.

300   We show the 68% and 95% confidence ellipses (joint probability) for each pair of equation of

301   state fit parameters as a function of pressure in Figure 5. Confidence ellipses, which are derived

302   from the fit-parameter covariance matrix, visualize magnitude and sign of parameter correlations

303   and provide insight into the acceptable parameter space. The primary correlation in a 3rd order

304   Birch-Murnaghan equation of state fit is between K_T and K'_T. As discussed in Angel (2000), this

305   parameter correlation is initially negative but continuously changes to a positive correlation with

306   pressure. Consequently, for every equation of state fit, there is some pressure where K_T and K'_T

307   are uncorrelated and uncertainties of the fit parameters are lowest. This pressure primarily

308   depends on the pressure range of a dataset but is also sensitive to the data distribution and

309   uncertainties. In our fits, the pressure where K_T and K'_T are uncorrelated is between 5 and 20

310   GPa, depending on the dataset. Above this pressure, K_T and K'_T are positively correlated, and

311   their uncertainties increase rapidly for pressures outside of the measured range.

312

313   In Figure 6, we present F-f plots for all our (Mg,Fe)O equation of state fits, with separate

314   subplots for samples compressed in helium, neon, and 4:1 methanol-ethanol pressure media. F-f

315   plots show normalized pressure (F) as a function of Eulerian strain (f), and can be useful for

316   estimating K_{0T} and K'_{0T} parameter values of a 3rd order Birch-Murnaghan equation of state. In an

317   F-f plot, if a straight line can be fit to a given dataset, its F-axis intercept corresponds to the

14

318   approximate value of K_{0T}. A positive or negative slope of the line indicates a value of K'_{0T} that is

319   either greater than or less than 4, respectively. A slope of zero means that K'_{0T} equals 4 which

320   effectively reduces the order and represents a 2nd order Birch-Murnaghan equation of state. If a

321   straight line does not properly model the F-f plot a higher-order equation of state is required to fit

322   the pressure-volume data. Specific results for each pressure medium will be discussed below.

323

324   The F-f plots of the samples in both helium and neon media show near-zero slopes, which

325   indicates a compositionally independent K'_{0T} value of about 4 that is consistent with observations

326   of low-Fe compositions with FeO $\leq$ 17 mol% from ultrasonic and Brillouin measurements. There

327   have been no high-pressure reports of both the compressional and shear velocities to compute the

328   bulk modulus, required for constraining a pressure derivative, for samples with greater iron

329   content. The positive F-f slopes in the samples compressed in 4:1 methanol-ethanol require a

330   different explanation, as this pressure medium is believed to remain hydrostatic to ~10 GPa

331   (Klotz et al. 2009). Jacobsen et al. (2005) speculated that they may be related to the limited

332   maximum compression of the samples or to differences between the quartz pressure scale and

333   others that are used more commonly (e.g. ruby fluorescence).

334

335   The F-intercepts on the F-f plots suggest a decrease in K_{0T} with increasing iron content for

336   samples compressed in helium and 4:1 methanol-ethanol, the pressure media in which the

337   compression of multiple (Mg,Fe)O compositions has been measured. These trends, with slopes

338   of about -0.15 GPa/mol%, are shown in Figure 7. Even though the trends have similar slopes, the

339   methanol-ethanol trend is offset in K_{0T} by about 3 GPa. It should be noted that the methanol-

340   ethanol K_{0T} values are not necessarily expected to be similar to those in other pressure media, as

341   these datasets cannot be fit with a K'$_{0T}$ near 4, and require a significantly higher value of ~5.5

342   (see Table 3). The best-fit K$_{0T}$ values of 163.0(1.0) GPa and 166(5) GPa for the cubic-indexed

343   Mw78 single crystal and powder in neon, respectively, are consistent with each other. They show

344   essentially the same result of K$_{0T}$ = 160(2) GPa and K'$_{0T}$ = 4.12(14) that was reported for

345   (Mg,Fe)O powder with 48 mol% FeO in neon using a spin-crossover equation of state

346   (Solomatova et al. 2016).

347

348   **Compositional Dependence of the Bulk Modulus (subsection)**

349   Values for K$_{0T}$ obtained from equation of state fits can also be compared to results using other

350   methods such as Brillouin spectroscopy and ultrasonic interferometry, which determine sound

351   velocities rather than density. Sound velocities and density are then combined to calculate the

352   adiabatic bulk modulus K$_S$, which is related to K$_T$ via K$_S$ = K$_T$ (1 + $\alpha\gamma$T), where α is the

353   volumetric thermal expansion coefficient, γ is the Grüneisen parameter, and T is temperature (in

354   our case, 298 K). Lack of sufficient data for the compositional dependence of $\alpha\gamma$ in the

355   (Mg,Fe)O system makes it unclear what values should be used, and therefore for Brillouin and

356   ultrasonic studies we are plotting K$_{0S}$.

357

358   As reported previously by Jacobsen et al. (2002), K$_{0S}$ trends differently for solid solutions

359   containing low and high Fe content. Crystals with FeO mol% up to ~15% show an increasing

360   K$_{0S}$ with increasing iron content, albeit with small-number statistics, while those with higher

361   FeO mol% show the opposite effect. This is in subtle contrast to equation of state fits to pressure-

362   volume data from diffraction, which support a linear decrease in K$_{0T}$ from MgO to Fe$_{1-x}$O. It

363   should be noted that this trend is observed for single crystals that likely have an increasing

16

364   amount of ferric iron towards the $Fe_{1-x}O$ end-member (this study, Jacobsen et al. 2002).

365   Additional work is needed to reconcile this discrepancy, with a potential focus on the differential

366   sensitivity of diffraction, ultrasonic, and Brillouin measurements to small proportions of a defect

367   structure.

368

369   **Implications**

370

371   In this paper, we studied the room-temperature elastic behavior of single-crystalline Mw78 in

372   helium and neon pressure media. We refined the compositional formula to $(Mg_{0.215}Fe_{0.762}\ _{0.023})O$

373   by constraining the ferric Fe content with high-resolution synchrotron Mössbauer spectroscopy.

374   As discussed earlier, iron-rich magnesiowüstite may be present in the Earth's core-mantle

375   boundary (CMB) region. An extrapolation of Mw78 elastic properties to pressure and

376   temperature conditions near the CMB requires additional information. The density of Mw78

377   resulting from the present study in helium has to be supplemented with thermal parameters such

378   as a pressure-dependent Debye temperature and Grüneisen parameter. Here we use $\theta_{D0} = 426$ K,

379    $\gamma_0 = 1.72(8)$, $q = 0.5$ as reported by Wicks et al. (2015) for $(Mg_{0.06}Fe_{0.94})O$, a composition similar

380   to that explored in the current study. We also assume the absence of phase transitions, as iron-

381   rich magnesiowüstite is expected to be cubic near the CMB (Fischer et al. 2011; Wicks et al.

382   2015). For the extrapolation of density, we use a Birch-Murnaghan Mie-Grüneisen equation of

383   state as implemented into the MINUTI software.

384

385   Pressure at the CMB is well established to be 135.8 GPa from the preliminary reference Earth

386   model (PREM) (Dziewonski and Anderson 1981), however, temperature at the CMB and the

387   temperature profile near the CMB are less well agreed on. Candidate geotherms from van der

388   Hilst et al. (2007) and Zhang et al. (2016) suggest that the upper bound for the core-mantle

389   boundary temperature is ~4000 K, but the addition of minor amounts of light elements will likely

390   depress this value. To compute geophysically-relevant parameters of crystalline Mw78 at the

391   CMB, we assume a CMB temperature of 3800 K (L. Zhang and Fei 2008; Fischer and Campbell

392   2010; Wicks et al. 2015; Kato et al. 2016). Extrapolating to the CMB pressure of 135.8 GPa at

393   300 K using the V_0, K_{0T}, and K'_{0T} parameters obtained from our single-crystal experiments in

394   neon and helium (Table 3), we obtain a density of 8.03(3) g/cm^3 for the sample in neon (using

395   the equation of state parameters from the cubic-indexed data set) and 8.17(3) g/cm^3 for the

396   sample in helium. The ~2% percent density difference between these two calculations is about a

397   factor of five higher than the uncertainty in density for the individual single-crystal equation of

398   state studies presented here. This illustrates the benefits of using an equation of state from high

399   quality measurements. Applying thermal considerations to compute the density at 3800 K at the

400   same pressure results in a density of 7.51 g/cm^3 using the equation of state of the sample in neon

401   and 7.63 g/cm^3 for the sample in helium.

402

403   To place the value for density computed from our study using a helium pressure medium in the

404   context of the 1D Earth model PREM, Mw78 is about 37% more dense than the average mantle

405   at the CMB. On the core side of the CMB, Mw78 is about 23% less dense than the outer core. If

406   magnesiowüstite with a similar composition to our sample existed above the core-mantle

407   boundary, it would form morphologies explored in work by Bower et al. (2011) that depend on a

408   small volume fraction mixed with silicates. It has recently been suggested that giant impacts over

409   Earth's history could have resulted in the temperature-dependent dissolution of small amounts of

18

410 Mg in the outer core, which then could have precipitated and floated to the core-mantle boundary

411 as the core cools, helping to drive the geodynamo over billions of years (O'Rourke and

412 Stevenson 2016). The precipitated Mg could react either with lower mantle material or any

413 oxygen present as a light element in the outer core, to form MgO (Badro et al. 2016) or

414 $(Mg,Fe)O$. As indicated by the density deficit of $(Mg_{0.22}Fe_{0.78})O$ compared with PREM, this

415 material could be emplaced on the core-side of the core-mantle boundary, potentially percolate

416 or diffuse into the lower mantle, and then stabilize at the base of the mantle.

417

418 To date, only a select number of $(Mg,Fe)O$ compositions have been investigated using single-

419 crystal diffraction at high pressure, and few Brillouin and ultrasonic studies exist with which to

420 compare the results. In this paper, we provided constraints on the elastic behavior of Mw78 in

421 helium and neon pressure media. From the significant differences of the corresponding

422 compression behavior, we conclude that nonhydrostaticity has a strong influence on the

423 appearance of distortions away from cubic symmetry in iron-rich $(Mg,Fe)O$ compositions. In

424 addition, the derived equations of state are clearly different, in particular at the high pressures

425 relevant to lower mantle conditions. The study of single crystals in a helium pressure medium

426 presents a valuable baseline upon which future studies can build, for example, by extending the

427 pressure range and elevating the temperature.

428

429 **Acknowledgements**

19

433   COMPRES. We are thankful for the single crystal sample provided to us by Stephen J.

434   Mackwell. We would like to thank Natalia Solomatova, Rachel Morrison, Przemek Dera, Jiyong

435   Zhao, Wenli Bi, Christine Beavers, Simon Teat, Vitali Prakapenka, Clemens Prescher, and

436   Sergey Tkachev for their assistance with our experiments.

437
438   **References**
439
440   Angel, R.J. (2000) Equations of state. Reviews in Mineralogy and Geochemistry, 41, 35–59.

441   Badro, J., Siebert, J., and Nimmo, F. (2016) An early geodynamo driven by exsolution of mantle
442   components from Earth's core. Nature, 536, 326–328.

443   Boehler, R., and De Hantsetters, K. (2007) New anvil designs in diamond-cells. High Pressure
444   Research, 24, 391–396.

445   Bower, D.J., Wicks, J.K., Gurnis, M., and Jackson, J.M. (2011) A geodynamic and mineral
446   physics model of a solid-state ultralow-velocity zone. Earth and Planetary Science Letters,
447   303, 193–202.

448   Bruker (2012a) APEX2. Bruker AXS Inc., Madison, Wisconsin, USA.

449   Bruker (2012b) CELL_NOW. Bruker AXS Inc., Madison, Wisconsin, USA.

450   Dera, P., Finkelstein, G.J., Duffy, T.S., Downs, R.T., Meng, Y., Prakapenka, V., and Tkachev, S.
451   (2013a) Metastable high-pressure transformations of orthoferrosilite Fs_{82}. Physics of the
452   Earth and Planetary Interiors, 221, 15–21.

453   Dera, P., Zhuravlev, K., Prakapenka, V., Rivers, M.L., Finkelstein, G.J., Grubor-Urosevic, O.,
454   Tschauner, O., Clark, S.M., and Downs, R.T. (2013b) High pressure single-crystal micro X-
455   ray diffraction analysis with GSE_ADA/RSV software. High Pressure Research, 1–19.

456   Dewaele, A., Loubeyre, P., and Mezouar, M. (2004) Equations of state of six metals above 94
457   GPa. Physical Review B, 70, 094112.

458   Dyar, M.D., Agresti, D.G., Schaefer, M.W., Grant, C.A., and Sklute, E.C. (2006) Mössbauer
459   spectroscopy of earth and planetary materials. dx.doi.org, 34, 83–125.

460   Dziewonski, A.M., and Anderson, D.L. (1981) Preliminary reference Earth model. Physics of the
461   Earth and Planetary Interiors, 25, 297–356.

462   Fei, Y., Wang, Y., and Finger, L.W. (1996) Maximum solubility of FeO in $(Mg, Fe)SiO_3$-
463   perovskite as a function of temperature at 26 GPa: Implication for FeO content in the lower
464   mantle. Journal of Geophysical Research, 101, 11525.

465   Finkelstein, G.J., Dera, P.K., Jahn, S., Oganov, A.R., Holl, C.M., Meng, Y., and Duffy, T.S.
466   (2014) Phase transitions and equation of state of forsterite to 90 GPa from single-crystal X-
467   ray diffraction and molecular modeling. American Mineralogist, 99, 35–43.

468   Fischer, R.A., and Campbell, A.J. (2010) High-pressure melting of wüstite. American
469   Mineralogist, 95, 1473–1477.

470   Fischer, R.A., Campbell, A.J., Shofner, G.A., Lord, O.T., Dera, P., and Prakapenka, V.B. (2011)
471   Equation of state and phase diagram of FeO. Earth and Planetary Science Letters, 304, 496–
472   502.

473   Hazen, R.M., and Jeanloz, R. (1984) Wüstite ($Fe_{1-x}O$): A review of its defect structure and
474   physical properties, 22, 37–46.

475   Irifune, T. (1994) Absence of an aluminous phase in the upper part of the Earth's lower mantle.

476   Jacobsen, S.D. (2002) Structure and elasticity of single-crystal (Mg,Fe)O and a new method of
477   generating shear waves for gigahertz ultrasonic interferometry. Journal of Geophysical
478   Research, 107, 2037.

479   Jacobsen, S.D., and Spetzler, H. (2004) Shear waves in the diamond-anvil cell reveal pressure-
480   induced instability in (Mg,Fe)O. Proceedings of the National Academy of Sciences of the
481   United States of America, 101, 5867–5871.

482   Jacobsen, S.D., Holl, C.M., Adams, K.A., Fischer, R.A., Martin, E.S., Bina, C.R., Lin, J.F.,
483   Prakapenka, V.B., Kubo, A., and Dera, P. (2008) Compression of single-crystal magnesium
484   oxide to 118 GPa and a ruby pressure gauge for helium pressure media. American
485   Mineralogist, 93, 1823–1828.

486   Jacobsen, S.D., Lin, J.-F., Angel, R.J., Shen, G., Prakapenka, V.B., Dera, P., Mao, H.-K., and
487   Hemley, R.J. (2005) Single-crystal synchrotron X-ray diffraction study of wüstite and
488   magnesiowüstite at lower-mantle pressures. Journal of Synchrotron Radiation, 12, 577–583.

489   Johnson, D.P. (1969) Mössbauer study of the local environments of ^{57}Fe in FeO. Solid State
490   Communications.

491   Kantor, I., Prakapenka, V., Kantor, A., Dera, P., Kurnosov, A., Sinogeikin, S., Dubrovinskaia,
492   N., and Dubrovinsky, L. (2012) BX90: A new diamond anvil cell design for X-ray
493   diffraction and optical measurements. Review of Scientific Instruments, 83.

494   Kantor, I.Y., McCammon, C.A., and Dubrovinsky, L.S. (2004) Mössbauer spectroscopic study
495   of pressure-induced magnetisation in wüstite (FeO). Journal of Alloys and Compounds, 376,
496   5–8.

497   Kato, C., Hirose, K., Nomura, R., Ballmer, M.D., Miyake, A., and Ohishi, Y. (2016) Melting in
498   the $FeO-SiO_2$ system to deep lower-mantle pressures: Implications for subducted banded
499   iron formations. Earth and Planetary Science Letters, 440, 56–61.

500   Klotz, S., Chervin, J.-C., Munsch, P., and Le Marchand, G. (2009) Hydrostatic limits of 11
501   pressure transmitting media. Journal of Physics D: Applied Physics, 42, 075413.

502   Lin, J.-F., Gavriliuk, A.G., Struzhkin, V.V., Jacobsen, S.D., Sturhahn, W., Hu, M.Y., Chow, P.,
503   and Yoo, C.-S. (2006) Pressure-induced electronic spin transition of iron in
504   magnesiowustite-(Mg,Fe)O. Physical Review B, 73, 113107.

505   Lin, J.F., Vanko, G., Jacobsen, S.D., Iota, V., Struzhkin, V.V., Prakapenka, V.B., Kuznetsov, A.,
506   and Yoo, C.S. (2007) Spin transition zone in earth's lower mantle. Science, 317, 1740–1743.

507   Mackwell, S., Bystricky, M., and Sproni, C. (2005) Fe–Mg interdiffusion in (Mg,Fe)O. Physics
508   and Chemistry of Minerals, 32, 418–425.

509   Manga, M., and Jeanloz, R. (1996) Implications of a metal-bearing chemical boundary layer in
510   D″ for mantle dynamics. Geophysical Research Letters.

511   Mao, H. (1997) Multivariable dependence of Fe-Mg partitioning in the lower mantle. Science,
512   278, 2098–2100.

513   Mao, W.L., Mao, H.-K., Sturhahn, W., Zhao, J., Prakapenka, V.B., Meng, Y., Shu, J., Fei, Y.,
514   and Hemley, R.J. (2006) Iron-rich post-perovskite and the origin of ultralow-velocity zones.
515   Science, 312, 564–565.

516   Mao, Z., Lin, J.-F., Liu, J., and Prakapenka, V.B. (2011) Thermal equation of state of lower-
517   mantle ferropericlase across the spin crossover. Geophysical Research Letters, 38.

518   McCammon, C.A., and Price, D.C. (1985) Mössbauer spectra of FexO (x>0.95). Physics and
519   Chemistry of Minerals, 11, 250–254.

520   Ohta, K., Fujino, K., Kuwayama, Y., Kondo, T., Shimizu, K., and Ohishi, Y. (2014) Highly
521   conductive iron-rich (Mg,Fe)O magnesiowüstite and its stability in the Earth's lower mantle.
522   Journal of Geophysical Research (Solid Earth), 119, 4656–4665.

523   O'Rourke, J.G., and Stevenson, D.J. (2016) Powering Earth's dynamo with magnesium
524   precipitation from the core. Nature, 529, 387–389.

525   Rivers, M., Prakapenka, V.B., Kubo, A., Pullins, C., Holl, C.M., and Jacobsen, S.D. (2008) The
526   COMPRES/GSECARS gas-loading system for diamond anvil cells at the Advanced Photon
527   Source. High Pressure Research, 28, 273–292.

528   Rost, S., Garnero, E.J., and Williams, Q. (2006) Fine-scale ultralow-velocity zone structure from
529   high-frequency seismic array data. Journal of Geophysical Research, 111, B09310.

530   Saines, P.J., Tucker, M.G., Keen, D.A., Cheetham, A.K., and Goodwin, A.L. (2013) Coupling of
531   the local defect and magnetic structure of wüstite Fe1−xO. Physical Review B, 88, 134418–
532   8.

533   Shu, J., Mao, H., Hu, J., and Fei, Y. (1998) Single-crystal X-ray diffraction of wüstite to 30 GPa

534   hydrostatic pressure. Neues Jahrbuch für Mineralogie Abhandlungen.

535   Sinmyo, R., Hirose, K., Nishio Hamane, D., Seto, Y., Fujino, K., Sata, N., and Ohishi, Y. (2008)
536   Partitioning of iron between perovskite/postperovskite and ferropericlase in the lower
537   mantle. Journal of Geophysical Research (Solid Earth), 113, B11204.

538   Solomatova, N.V., Jackson, J.M., Sturhahn, W., Wicks, J.K., Zhao, J., Toellner, T.S., Kalkan, B.,
539   and Steinhardt, W.M. (2016) Equation of state and spin crossover of (Mg,Fe)O at high
540   pressure, with implications for explaining topographic relief at the core-mantle boundary.
541   American Mineralogist, 101, 1084–1093.

542   Struzhkin, V.V., Mao, H.-K., Hu, J., Schwoerer-Böhning, M., Shu, J., Hemley, R.J., Sturhahn,
543   W., Hu, M.Y., Alp, E.E., Eng, P., and others (2001) Nuclear inelastic x-ray scattering of FeO
544   to 48 GPa. Physical Review Letters, 87, 255501–4.

545   Sturhahn, W. (2015a) CONUSS (COherent NUclear resonant Scattering by Single crystals) open
546   source software. www.nrixs.net.

547   Sturhahn, W. (2015b) MINUTI (MINeral physics UTIlities) open source software.
548   www.nrixs.net.

549   Sun, D., Helmberger, D.V., Jackson, J.M., Clayton, R.W., and Bower, D.J. (2013) Rolling hills
550   on the core–mantle boundary. Earth and Planetary Science Letters, 361, 333–342.

551   Thorne, M.S., and Garnero, E.J. (2004) Inferences on ultralow-velocity zone structure from a
552   global analysis of SPdKS waves. Journal of Geophysical Research.

553   Toellner, T.S. (2000) Monochromatization of synchrotron radiation for nuclear resonant
554   scattering experiments. Hyperfine Interactions, 125, 3–28.

555   Tschauner, O., Ma, C., Beckett, J.R., Prescher, C., Prakapenka, V.B., and Rossman, G.R. (2014)
556   Discovery of bridgmanite, the most abundant mineral in Earth, in a shocked meteorite.
557   Science, 346, 1100–1102.

558   Van der Hilst, R.D., De Hoop, M.V., Wang, P., Shim, S.H., Ma, P., and Tenorio, L. (2007)
559   Seismostratigraphy and thermal structure of Earth's core-mantle boundary region. Science,
560   315, 1813–1817.

561   Welberry, T.R., and Christy, A.G. (1997) Defect distribution and the diffuse X-ray diffraction
562   pattern of wustite, $Fe_{1-x}O$. Physics and Chemistry of Minerals, 24, 24–38.

563   Wen, L. (1998) Ultra-Low Velocity Zones Near the Core-Mantle Boundary from Broadband
564   PKP Precursors. Science, 279, 1701–1703.

565   Westrenen, W.V., Li, J., Fei, Y., Frank, M.R., Hellwig, H., Komabayashi, T., Mibe, K., Minarik,
566   W.G., Orman, J.A.V., Watson, H.C., and others (2005) Thermoelastic properties of
567         $(Mg_{0.64}Fe_{0.36})O$ ferropericlase based on in situ X-ray diffraction to 26.7GPa and 2173K.
568   Physics of the Earth and Planetary Interiors, 151, 163–176.

569   Wicks, J.K., Jackson, J.M., and Sturhahn, W. (2010) Very low sound velocities in iron-rich
570   (Mg,Fe)O: Implications for the core-mantle boundary region. Geophysical Research Letters,
571   37.

572   Wicks, J.K., Jackson, J.M., Sturhahn, W., and Zhang, D. (2017) Sound velocity and density of
573   magnesiowüstites: Implications for ultralow-velocity zone topography. Geophysical
574   Research Letters.

575   Wicks, J.K., Jackson, J.M., Sturhahn, W., Zhuravlev, K.K., Tkachev, S.N., and Prakapenka, V.B.
576   (2015) Thermal equation of state and stability of (Mg$_{0.06}$Fe$_{0.94}$)O. Physics of the Earth and
577   Planetary Interiors, 249, 28–42.

578   Williams, Q., Revenaugh, J., and Garnero, E. (1998) A correlation between ultra-low basal
579   velocities in the mantle and hot spots. Science, 281, 546–549.

580   Zhang, D., Jackson, J.M., Zhao, J., Sturhahn, W., Alp, E.E., Hu, M.Y., Toellner, T.S., Murphy,
581   C.A., and Prakapenka, V.B. (2016) Temperature of Earth's core constrained from melting of
582   Fe and Fe$_{0.9}$Ni$_{0.1}$ at high pressures. Earth and Planetary Science Letters, 447, 72–83.

583   Zhang, D., Jackson, J.M., Zhao, J., Sturhahn, W., Alp, E.E., Toellner, T.S., and Hu, M.Y. (2015)
584   Fast temperature spectrometer for samples under extreme conditions. Review of Scientific
585   Instruments, 86, 013105.

586   Zhang, L., and Fei, Y. (2008) Melting behavior of (Mg,Fe)O solid solutions at high pressure.
587   Geophysical Research Letters, 35.

588   Zhuravlev, K.K., Jackson, J.M., Wolf, A.S., Wicks, J.K., Yan, J., and Clark, S.M. (2010)
589   Isothermal compression behavior of (Mg,Fe)O using neon as a pressure medium. Physics
590   and Chemistry of Minerals, 37, 465–474.

591

592   **Figure Captions**

593

594   Figure 1. Pseudo-precession *hk0* image of Mw78 diffraction at ambient conditions collected in

595   air at ALS. Weak satellite peaks and diffuse scattering can be seen around the main Bragg

596   reflections.

597

598   Figure 2. Synchrotron Mössbauer spectrum of Mw78 single crystal at room pressure.

24

599   The raw data and associated 1σ error bars are shown as light-gray markers, and the best-fit

600   model is shown as a purple line. The inset shows the calculated energy spectrum using the best-

601   fit parameters from the measured time spectrum and the contributions to the fit from each

602   individual site (pink, red, blue, and green correspond to the Fe_A^{2+}, Fe_B^{2+}, Fe_C^{2+}, and Fe_D^{3+} sites

603   described in Table 1). In this calculation the absolute isomer shift is arbitrary, and only the

604   relative isomer shift is meaningful.

605

606   Figure 3. a) Top: Ruby standard deviation as a function of mean ruby pressure for both helium-

607   (orange circles) and neon-loaded (cyan circles) diamond anvil cells. Bottom: *c/a* ratio as a

608   function of mean ruby pressure for both helium- (orange circles) and neon-loaded (cyan circles)

609   diamond anvil cells. Uncertainty in pressure is represented as one ruby standard deviation. Error

610   bars are not given for the ruby standard deviation, and, when not visible, other error bars are

611   smaller than the symbol size. Uncertainty in pressure is represented as one ruby standard

612   deviation, and error in *c/a* ratio represents a 1σ uncertainty that has been propagated from lattice

613   parameter fits. When not visible, error bars are smaller than the symbol size. b) The reciprocal

614   lattice of the single-crystal in neon at 53.3 GPa. Red vectors outline the hexagonal unit cell and

615   its relationship to a pseudo-cubic unit cell.

616

617   Figure 4. Normalized unit cell volumes of Mw78 and equations of state fit using MINUTI

618   (Sturhahn 2015b). Orange, dark cyan/green, and light cyan symbols correspond to diffraction

619   from a single crystal of Mw78 in helium (this study, indexed using a cubic unit cell), a single

620   crystal of Mw78 in neon (this study, indexed using a cubic unit cell below and a hexagonal unit

621   cell above 20 GPa), and powdered $(Mg_{0.22}Fe_{0.78})O$ in neon (Zhuravlev et al. 2010), respectively.

25

622   Circles represent measured unit cell volumes normalized by the zero-pressure unit cell volume

623   resulting from a fit by a 3rd order Birch-Murnaghan equation of state. Uncertainty in pressure is

624   represented as one ruby standard deviation. Shaded regions represent the fit 3rd order Birch-

625   Murnaghan equations of state with 1σ fitting errors. Where not visible, vertical error bars on

626   individual data points are smaller than the symbol size.

627

628   Figure 5. a) Confidence ellipses of K_T and K'_T at 68% and 95% levels for several (Mg,Fe)O

629   compositions at 0, 20, and 130 GPa. Orange, cyan, and brown ellipses represent diffraction

630   measurements in helium, neon, and 4:1 methanol-ethanol pressure media (Jacobsen 2002;

631   Jacobsen et al. 2005; 2008; Zhuravlev et al. 2010), respectively. Darker ellipses correspond to

632   samples from this study (the ellipses corresponding to the sample in Ne are derived from the

633   covariance matrix of the equation of state fit to the low-pressure cubic-indexed data points). b)

634   Confidence ellipses of V and K_T. c) Confidence ellipses of V and K'_T.

635

636   Figure 6. Plots of normalized pressure (F) as a function of Eulerian strain (f) corresponding to

637   compression data (filled circles with error bars) and equation of state fits (solid lines) for various

638   (Mg,Fe)O compositions (Jacobsen 2002; Jacobsen et al. 2005; 2008; Zhuravlev et al. 2010). Top:

639   Single-crystal studies in a helium pressure medium. Middle. Single-crystal and powder studies in

640   a neon pressure medium. Dark green and dark cyan data points are from the same sample, and

641   represent fits to the portions of the data that can be indexed using cubic and hexagonal unit cells,

642   respectively. For the data from the samples in a neon pressure medium, a strong prior was placed

643   on K'_{0T}, causing it to stay near a value of 4.0 ± 0.1 during fitting. Bottom: Single-crystal studies

644   in a 4:1 methanol-ethanol pressure medium. Dark symbols/lines correspond to data collected for

26

645   this study and light symbols/lines correspond to previous studies. The error bars in F and f

646   correspond to 1σ uncertainties, and when not visible, are smaller than the symbol size (see Angel

647   (2000) for details on F-f plot error bar calculations). Uncertainties are not given for the lines

648   corresponding to the equation of state fits.

649

650   Figure 7. K_{0T} (diffraction) and K_{0S} (ultrasonic, Brillouin) compositional trends for (Mg,Fe)O

651   solid solutions from single-crystal studies. Ultrasonic and Brillouin studies are represented by

652   red and purple symbols, respectively. Single-crystal diffraction studies in helium, neon, and 4:1

653   methanol-ethanol pressure media are represented by orange, cyan, and brown symbols,

654   respectively. The dashed lines show weighted linear least-square fits to the data. In the equations

655   that correspond to the best-fit lines, x is the iron mol% and y is either K_{0T} (diffraction) or K_{0S}

656   (ultrasonic, Brillouin) in units of GPa. Compositional error bars are smaller than the symbol size

657   and K_0 error bars are either 1σ uncertainties from equation of state fitting (diffraction) or those

658   reported in the literature (Brillouin, ultrasonic).

659

Table 1. Mw78 room-pressure best-fit hyperfine parameters

Site	Coordination Environment	Weight Fraction (%)	IS (mm/s)	QS (mm/s)	FWHM (mm/s)
Fe_A^{2+}	Octahedral	69.7(1.0)	1.0^b	0.592(3)	$0.1319(14)^c$
Fe_B^{2+}	Octahedral	17.3(1.0)	1.0^b	0.913(5)	$0.1319(14)^c$
Fe_C^{2+}	Octahedral	7 [a]	1.0^b	1.307(7)	$0.1319(14)^c$
Fe_D^{3+}	Tetrahedral	6 [a]	0.044(10)	0	0.427(12)

Thickness = 137.6(1.3) μm, Lamb Mössbauer Factor = 0.75
IS = Isomer Shift, QS = Quadrupole Splitting, FWHM = Full-Width at Half Maximum
[a]These site fractions were manually varied to optimize the fit.
[b]The isomer shift for these sites was fixed so that the relative isomer shift for the ferric Fe site could be reported.
[c]The widths of the doublet sites were constrained to be identical to each other.

Table 2. Lattice parameters and unit cell volumes of Mw78

	Ambient – Cubic Unit Cell	
P (GPa)	a (Å)	V (Å^3)
0.0001	4.2898(4)*	78.94(2)

		Helium Medium – Cubic Unit Cell		
Ruby 1 λ (nm)	Ruby 2 λ (nm)	Avg. P (GPa)	a (Å)	V (Å^3)
694.95	694.95	1.823(16)	4.2703(12)	77.87(7)
696.13	696.14	5.128(32)	4.2433(12)	76.40(7)
697.41	697.45	8.786(63)	4.2132(12)	74.79(7)
698.64	698.67	12.294(64)	4.1860(13)	73.35(7)
699.98	700.01	16.199(65	4.1596(13)	71.97(7)
701.02	701.06	19.301(72)	4.1420(12)	70.97(7)
702.29	702.33	23.119(75)	4.1152(15)	69.69(8)
703.38	703.44	26.467(115)	4.1003(11)	68.94(6)
704.22	704.28	29.044(136)	4.0838(14)	68.11(7)
705.13**	705.15	31.820(52)	4.0707(13)	67.46(7)
706.40	706.44	35.856(86)	4.0491(13)	66.38(7)
707.70	707.74	40.004(94)	4.0314(15)	65.52(7)
708.40	708.46	42.319(127)	4.0235(13)	65.12(7)
709.73	709.77	46.645(71)	4.0034(11)	64.16(5)
710.78	710.84	50.177(145)	3.9891(15)	63.48(8)
711.48	711.53	52.517(129)	3.9781(14)	62.95(7)
712.35	712.44	55.542(222)	3.9665(16)	62.40(8)

	Helium Medium – Hexagonal Unit Cell			
Avg. P (GPa)	a (Å)	c (Å)	c/a	V (Å^3)
1.823(16)	3.0184(17)	7.404(10)	2.453(4)	58.42(10)
5.128(32)	3.0011(16)	7.345(9)	2.448(4)	57.29(9)
8.786(63)	2.9778(16)	7.307(10)	2.454(4)	56.11(10)
12.294(64)	2.9592(17)	7.255(10)	2.452(4)	55.02(10)
16.199(65	2.9388(14)	7.221(9)	2.457(4)	54.01(8)
19.301(72)	2.9265(16)	7.179(10)	2.453(4)	53.24(9)
23.119(75)	2.9063(18)	7.151(10)	2.461(4)	52.31(10)
26.467(115)	2.8994(14)	7.102(8)	2.449(3)	51.70(8)
29.044(136)	2.8858(19)	7.086(11)	2.455(5)	51.10(11)
31.820(52)	2.8761(17)	7.067(10)	2.457(4)	50.63(10)
35.856(86)	2.8620(17)	7.021(10)	2.453(4)	49.80(10)
40.004(94)	2.8490(19)	6.993(11)	2.455(5)	49.16(11)
42.319(127)	2.8418(16)	6.991(10)	2.460(4)	48.89(9)
46.645(71)	2.8295(13)	6.953(15)	2.457(6)	48.21(11)
50.177(145)	2.820(2)	6.914(12)	2.452(5)	47.62(11)
52.517(129)	2.8110(19)	6.903(11)	2.456(5)	47.24(10)
55.542(222)	2.8008(19)	6.898(12)	2.463(5)	46.86(10)

	Neon Medium – Cubic Unit Cell			

Ruby 1 λ (nm)	Ruby 2 λ (nm)	Avg. P (GPa)	a (Å)	V (Å³)
694.76	694.77	1.314(20)	4.2749(5)	78.12(3)
696.19	696.20	5.294(20)	4.2423(5)	76.35(3)
697.51	697.52	9.029(21)	4.2162(5)	74.95(3)
699.12	699.14	13.682(42)	4.1827(5)	73.18(3)
701.02	701.02	19.244	4.1505(6)	71.5(4)
702.73	702.53	24.084(43)	4.1246(8)	70.17(5)
704.45	704.07	29.081(84)	4.1023(13)	69.04(7)
706.12	705.66	34.18(1.03)	4.0806(15)	67.95(8)
708.20	707.68	40.73(1.19)	4.0546(19)	66.66(10)
709.14	708.66	43.86(1.12)	4.039(3)	65.90(15)
710.26	709.73	47.46(1.25)	4.028(3)	65.36(15)
712.03	711.43	53.28(1.44)	4.003(4)	65.14(20)

<div align="center">Neon Medium – Hexagonal Unit Cell</div>

Avg. P (GPa)	a (Å)	c (Å)	c/a	V (Å³)
1.314(20)	3.0240(7)	7.409(3)	2.4500(12)	58.68(4)
5.294(20)	3.0000(8)	7.347(3)	2.4490(12)	57.26(4)
9.029(21)	2.9813(8)	7.304(3)	2.4499(13)	56.22(4)
13.682(42)	2.9581(7)	7.243(3)	2.4485(12)	54.89(4)
19.244	2.9318(8)	7.201(3)	2.4562(13)	53.60(4)
24.084(43)	2.9102(9)	7.170(4)	2.4637(16)	52.59(5)
29.081(84)	2.8891(12)	7.152(5)	2.476(3)	51.79(6)
34.18(1.03)	2.8720(13)	7.122(5)	2.480(3)	50.88(6)
40.73(1.19)	2.8508(16)	7.086(6)	2.486(3)	49.87(8)
43.86(1.12)	2.833(2)	7.092(9)	2.503(4)	49.29(10)
47.46(1.25)	2.8214(18)	7.084(7)	2.511(3)	48.83(8)
53.28(1.44)	2.7953(18)	7.070(7)	2.529(3)	47.84(8)

* Using the relationships $a_{hex} = a_{cubic}/\sqrt{2}$ and $c_{hex} = \sqrt{3}\, a_{cubic}$ to transform cubic to hexagonal resulting in $a_{hex} = 3.0333$ Å and $c_{hex} = 7.4302$ Å and $V_{hex} = 59.21$ Å³.

**Ruby 1 was not measured at this pressure point. To estimate a pressure comparable with the other data points, we used the other data points to fit the ruby 1 wavelength as a linear function of ruby 2 wavelength. The resulting equation, which we used to estimate the ruby 1 pressure (P_{ruby1}), was: $P_{ruby1} = 0.9973*P_{ruby2} + 1.8804$ (GPa). P_{ruby1} and P_{ruby1} are in units of GPa.

Table 3. Selected 300 K (Mg,Fe)O Equation of State Fit Parameters

Work[**]	Composition	Medium	Technique	P Range (GPa)	V_0 (Å^3)	K_{0T} (GPa)	K'_{0T}
Jacobsen et al. (2005)	$Fe_{0.93}O$	Helium	SXRD	0-22.8	79.41(4)	145.7(1.2)	3.99(6)[b]
				Published Fit:	*79.41(4)*	*146(2)*	*4.0 (fixed)*
This Study (cubic)	$(Mg_{0.22}Fe_{0.78})O$	Helium	SXRD	1.8-55.5	78.87(6)[a]	148(3)	4.09(12)
This Study (cubic)	$(Mg_{0.22}Fe_{0.78})O$	Neon	SXRD	1.3-19.2	78.742(14)[a]	163.0(1.0)	4.02(10)[b]
This Study (hex.)	$(Mg_{0.22}Fe_{0.78})O$	Neon	SXRD	24.1-53.3	58.7(4)	176.8(1.1)	4.00(10)[b]
Zhuravlev et al. (2010)	$(Mg_{0.22}Fe_{0.78})O$	Neon	PXRD	7.9-39.8	78.5(2)	166(5)	4.01(10)[b]
				Published Fit:	*78.49(21)*	*166(5)*	*4.0 (fixed)*
Jacobsen et al. (2002)	$(Mg_{0.25}Fe_{0.75})O$	4:1 Meth-Eth	SXRD	0-7.2	78.082(3)	151.3(7)	5.6(2)
				Published Fit:	*78.082(3)*	*151.3(6)*	*5.55(19)*
Jacobsen et al. (2002)	$(Mg_{0.44}Fe_{0.56})O$	4:1 Meth-Eth	SXRD	0-8.9	77.457(4)	155.2(8)	5.7(3)
				Published Fit:	*77.453(4)*	*155.8(9)*	*5.5(2)*
Jacobsen et al. (2002)	$(Mg_{0.73}Fe_{0.27})O$	4:1 Meth-Eth	SXRD	0-9.3	76.336(3)	158.4(5)	5.48(11)
				Published Fit:	*76.336(3)*	*158.4(4)*	*5.49(11)*
Jacobsen et al. (2005)	$(Mg_{0.73}Fe_{0.27})O$	Helium	SXRD	0-51.1	77.30(4)	154.8(1.9)	3.97(10)
				Published Fit:	*76.30(9)*	*154(3)*	*4.0(1)*
Jacobsen et al. (2008)	MgO	Helium	SXRD	0-118.1	74.707(5)	160.08(14)	4.030(4)
				Published Fit:	*74.697(6)*	*160.2**	*4.03**

* From (2000) MgO primary pressure scale
** If symmetry is not noted, the datasets represent cubic forms of (Mg,Fe)O
[a] Prior of V_0 = 78.94±0.1 Å^3 used during equation of state fit
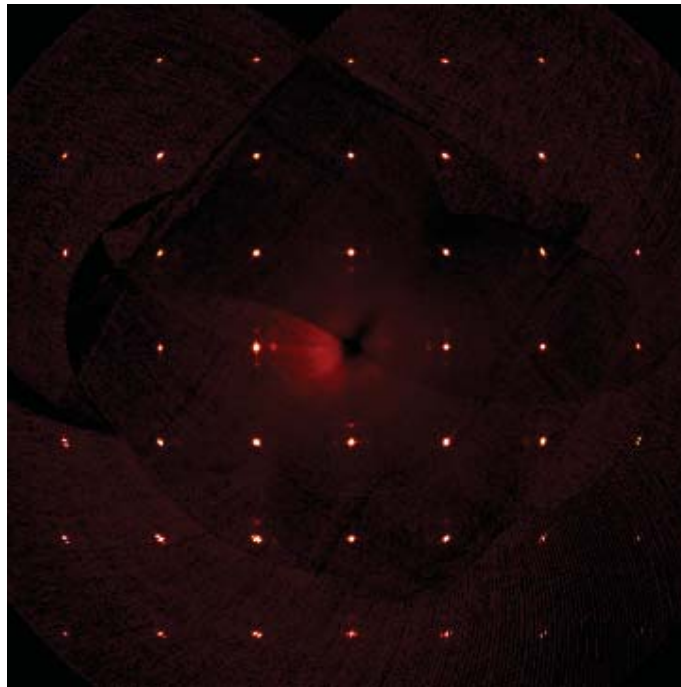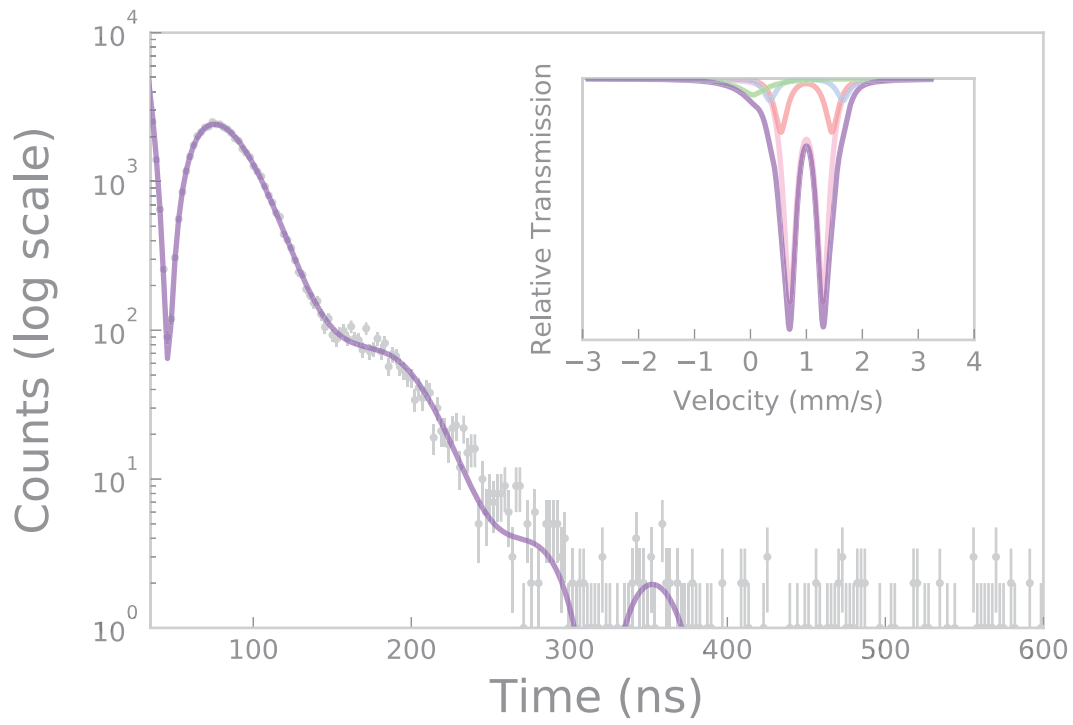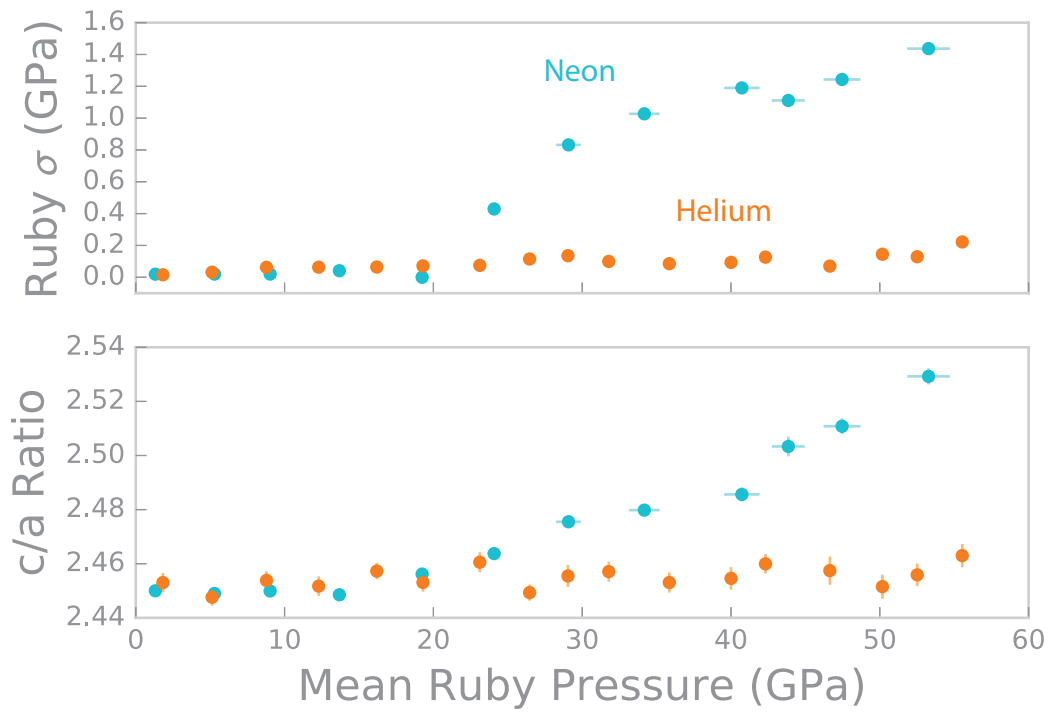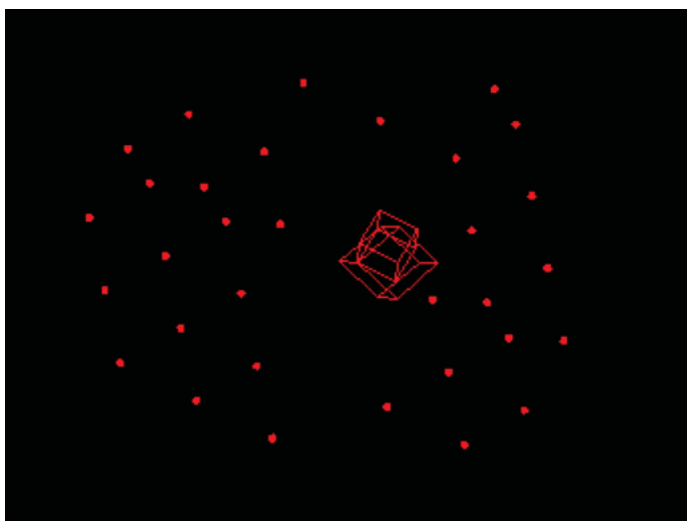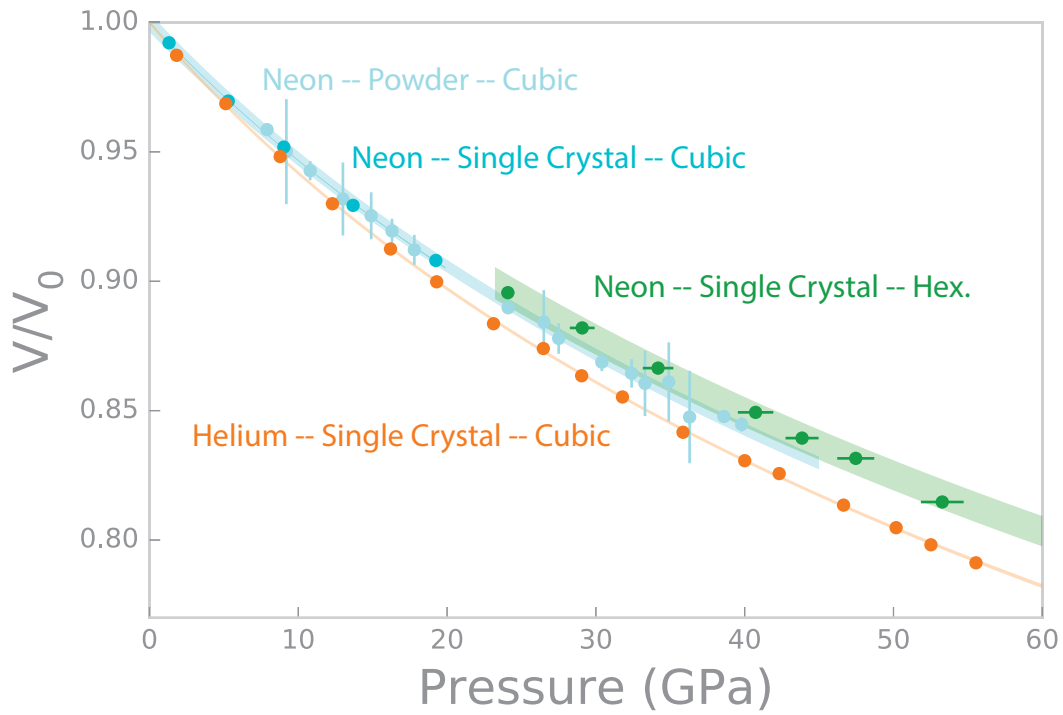[b] Prior of K'_{0T} = 4.0±0.1 used during equation of state fit
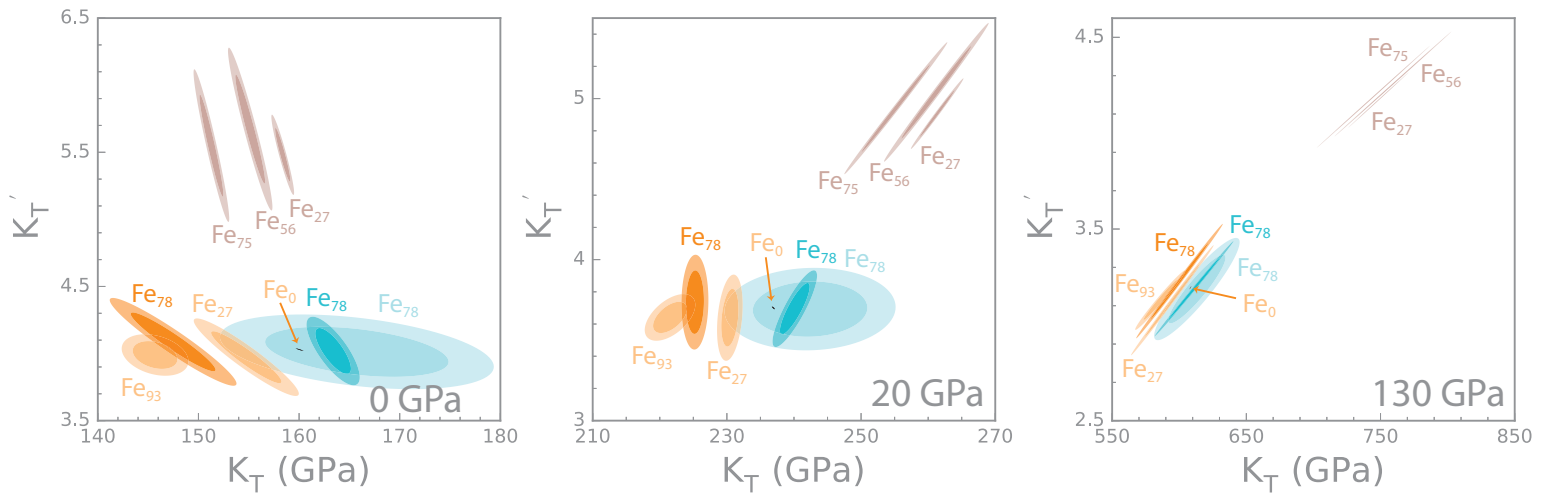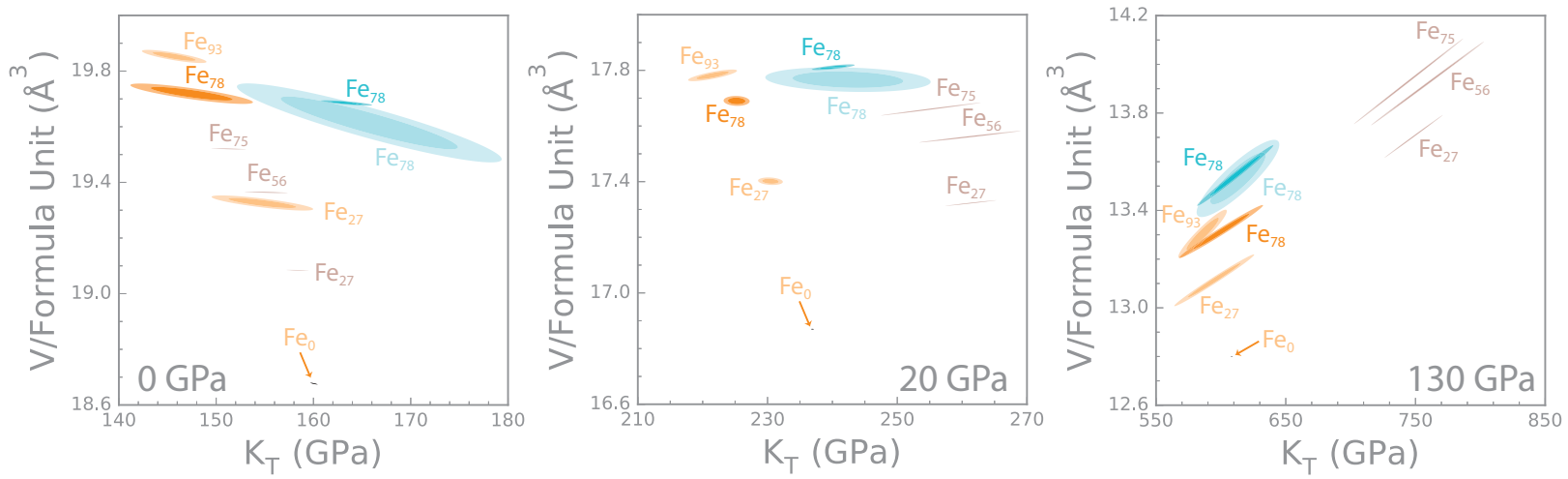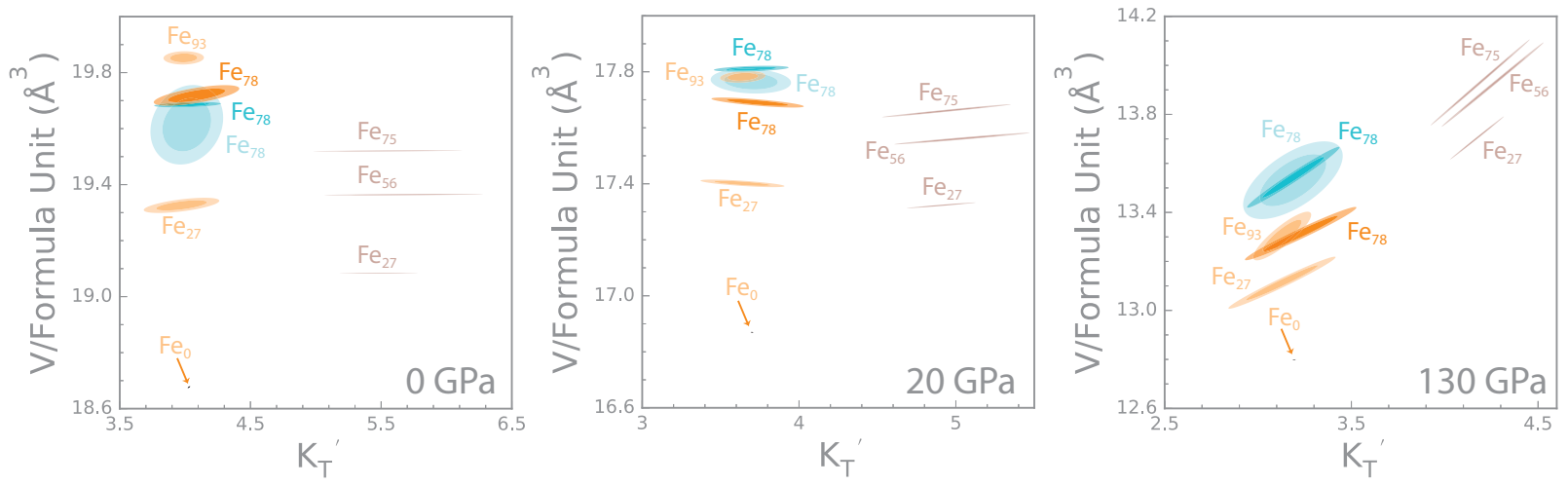
Figure 1

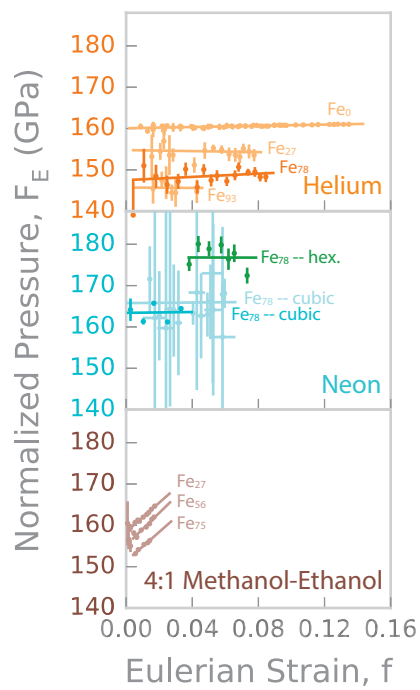Figure 2

Figure 3a

Figure 3b

Figure 4

Figure 5a

Figure 5b

Figure 5c

Figure 6

Figure 7